ADVANCED FUNCTIONAL MATERIALS
www.afm-journal.de

Magnesium-Ion Battery Anode from Polymer-Derived SiOC Nanobeads

Wuqi Guo, Oyku Icin, Cekdar Vakifahmetoglu, Delf Kober, Aleksander Gurlo, and Maged F. Bekheet*

Tin-containing silicon oxycarbide (SiOC/Sn) nanobeads are synthesized with different carbon/tin content and tested as electrodes for magnesium-ion batteries. The synthesized ceramics are characterized by thermogravimetric-mass spectroscopy, Fourier-transform infrared spectroscopy, X-ray diffraction (XRD), Raman spectroscopy, N_2 sorption analysis, scanning electron microscope, energy-dispersive X-ray, and elemental analysis. Galvanostatic cycling tests, rate performance tests, electrochemical impedance spectroscopy (EIS), cyclic voltammetry (CV) tests, and ex situ XRD measurements are conducted. Results of battery performance tests present a high capacity of 198.2 mAh g^{-1} after the first discharging and a reversible capacity of 144.5 mAh g^{-1} after 100 cycles at 500 mA g^{-1}. Excellent rate performance efficiency of 85.2% is achieved. Battery performances in this research are influenced by surface area, and tin contentof the SiOC/Sn nanobeads. EIS, CV tests, and ex situ XRD measurements reveal that higher surface area contributes to higher capacity by providing more accessible Mg^{2+} ion storage sites and higher rate capability by improving the diffusion process. Higher Sn content increases battery capacity through reversible Mg-Mg_2Sn-Mg alloying/dealloying process and improves the rate performances by increasing electrical conductivity. Besides, SiOC advances cycling stability by preventing electrode collapse and enhances the capacity due to higher surface capacitive effects.

1. Introduction

Lithium-ion batteries (LIBs) are essential power sources in our daily life. Graphite with a theoretical capacity of 372 mAh g^{-1} is usually practiced as the anode in LIBs.[1] But such capacity cannot meet the high energy demands. One promising anode material for LIBs is silicon (Si), with a theoretical capacity of around 3600 mAh g^{-1}, i.e., nearly ten times that of graphite.[2] However, the use of silicon anodes remains limited because of significant volume expansion and pulverization during battery cycling, leading to structural deterioration and poor performance stability.[3] Polymer-derived ceramics (PDCs), mainly with Si-backbone, can be an excellent candidate to remedy the problems mentioned.[4] Of those, silicon oxycarbide (SiOC), with silicon tetrahedrally coordinated to oxygen and carbon, has already been investigated as electrodes in rechargeable LIBs.[3,5–8] This material can easily be produced on a large scale by the pyrolysis of polysiloxane preceramic polymers.[9,10] What is believed in SiOC is that the microstructure with a silica-rich network and carbon phase results in particular viscoelastic behavior, which is beneficial for preventing large expansion and contraction during battery cycling.[11] Besides the SiOC ceramic network, the free carbon precipitates in SiOC provide active sites for ion storage and may increase electrical conductivity.[12]

Generally speaking, due to low electrical conductivity, additives are provided to improve the reversible capacity, cycling stability, and rate performance of SiOC electrodes.[13] One such additive is metallic tin with a theoretical capacity of 994 mAh g^{-1} (for Li-ion storage) and a high electrical conductivity of 91 000 S cm^{-1}.[14] It was shown for the Li-ion batteries that the higher reversible capacity was obtained in the first cycles when Sn was present in the tested anode. In addition, it is known that Sn contributes to crosslinking of some siloxane precursors.[11] It should also be underlined that, like Si electrodes, metallic Sn electrodes suffer from intense volume expansion and particle aggregation, leading to poor cycling stability.[15] Thus, SiOC ceramics are suitable active matrices to buffer volume change and agglomeration of Sn during battery cycling.[12,16–18]

W. Guo, D. Kober, A. Gurlo, M. F. Bekheet
Technische Universität Berlin
Faculty III Process Sciences, Institute of Materials Science and Technology
Chair of Advanced Ceramic Materials
Straße des 17. Juni 135, 10623 Berlin, Germany
O. Icin, C. Vakifahmetoglu
Department of Materials Science and Engineering
Izmir Institute of Technology
Urla, Izmir 35430, Turkey
E-mail: cekdarvakifahmetoglu@iyte.edu.tr

The ORCID identification number(s) for the author(s) of this article can be found under https://doi.org/10.1002/adfm.202304933

DOI: 10.1002/adfm.202304933

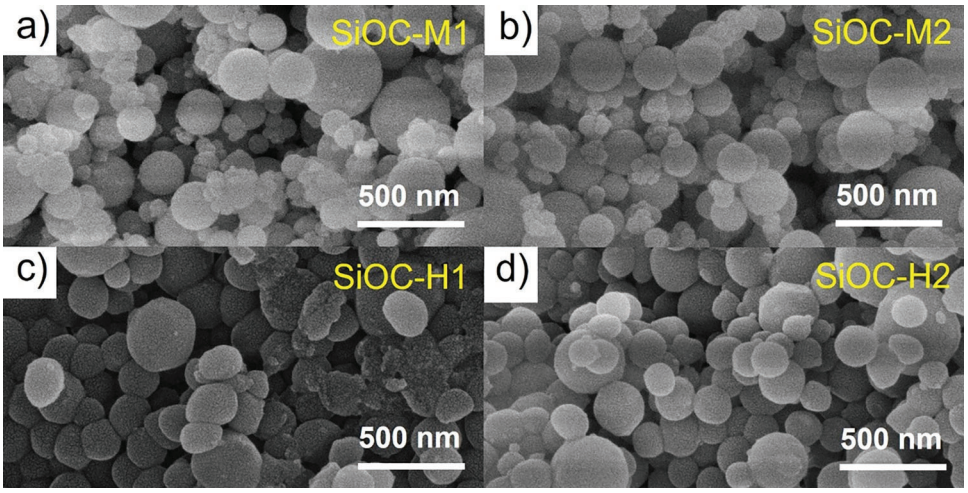

Figure 1. SEM images of a) SiOC-M1, b) SiOC-M2, c) SiOC-H1, and d) SiOC-H2 nanobeads.

In contrast to lithium, whose sources are of limited geological availability, magnesium has a high abundance in the Earth's crust (≈2 wt%).[19] Considering the battery performance, magnesium as an electrode possesses advantages, including a high theoretical volumetric energy density of 3832 mAh mL^{-1} (vs 2046 mAh mL^{-1} for Li-metal anode) and a high gravimetric capacity of 2205 mAh g^{-1}, alongside a lower tendency for anodic dendrite formation, alleviating one of the critical safety concerns associated with Li-ion batteries.[20] Besides, magnesium electrodes have a negative reduction potential of −2.3 V versus a standard hydrogen electrode.[21]

It is pertinent to note that Si-based inorganic materials have been extensively tested for LIBs over the previous few decades.[3] However, the same is not the case for magnesium. Similarly, although Si-based PDCs have already been studied as electrodes in rechargeable LIBs,[4] there are no reports to explore their potential for MIBs. One of the most significant advantages of applying the synthesized tin-containing SiOC nanobeads as anodes/cathodes in magnesium batteries is they provide several potential Mg ion storage ways in a stable SiOC matrix with free carbon, enhanced electrical conductivity from Sn and surface area from the nanobeads morphology. Besides, homogenously distributed tin particles can be immobilized in the SiOC matrix, which prevents their tendency to form agglomeration under battery cycling.[12,17] The Mg insertion might also result in the cleavage of some Si—C or Si—O bonds in the SiOC matrix and the expansion, providing favorable sites for the subsequent ion insertion in the network. At the same time, the Mg^{2+} ions could react rapidly with a metal tin, free carbon, and possibly Si to form different Mg-based alloys such as Mg_2Sn, Mg_xC, and Mg-Si.

In this context, spherical SiOC/Sn nanobeads were synthesized with different C/Sn content via facile oil in water (o/w) emulsion technique; in addition, irregular particles having the same composition but lower surface area were also synthesized for comparison. Following in-depth characterization, samples were evaluated for their performance correlated with chemical composition (carbon/tin) differences and particle characteristics (surface area/particle shape) to validate their potential for the first time in magnesium batteries.

2. Results and Discussion

Figure 1 presents scanning electron microscope (SEM) images of the synthesized SiOC-M1 & M2, SiOC-H1 & H2 samples, and corresponding energy-dispersive X-ray (EDX) mappings are given in Figure S1 (Supporting Information). Although all four samples consist of spherical sub-micrometer sized beads, they differ slightly in their size and shape regularity. The nanobeads in the SiOC-M set possess ideal spherical shapes with broader distribution, while SiOC-H samples consist of somewhat nonideal spherical nanobeads with narrow size distribution. The average spherical size of the SiOC-M samples was measured as 280 ± 140 nm, very close to the value for the SiOC-H set with 285 ± 90 nm (Figure S2, Supporting Information). While poly(methylsiloxane) (PMS) has ≈4 mole % reactive groups (—OH and C_2H_5), poly(methyl-phenyl-siloxane) (PMPS) includes 7–10 mole% of those contributing further for crosslinking behavior,[22] resulting in a narrower particle size distribution since the thermoset bead morphology was set earlier. Transmission electron microscopy (TEM) characterization of SiOC-M2 (**Figure 2**a–c) and SiOC-H2 (Figure 2d,e) samples confirms the results of SEM characterization and shows the homogeneous distribution of spherical crystalline Sn nanoparticles within the amorphous ceramic matrices. The Sn nanoparticles in the SiOC-M2 sample have a particle size with an average diameter of 29.9 ± 5 nm. In contrast, the SiOC-H2 sample contains many ultrafine Sn particles with sizes below 10 nm and a few with larger sizes due to the particle agglomerations. The uniform particle size distribution and low extent of agglomeration observed in the SiOC-M2 sample might be explained by the encapsulation of the Sn nanoparticles by protective layers of turbostratic carbon, which is indicated by its interplanar distance of $d_{002} \approx 0.34$ nm (see Figure 2c). The presence of metallic Sn in SiOC matrix is confirmed from the interplanar distance of $d_{101} \approx 0.279$ nm and SAED pattern (inset of Figure 2c) showing diffraction ring corresponding to the lattice planes of its tetragonal structure (space group $I4_1/amd$).

As shown in Figure S3a (Supporting Information), the N_2 physisorption isotherms of the SiOC-M1 and SiOC-M2 samples derived from PMS polymer exhibit reversible Type IV isotherms

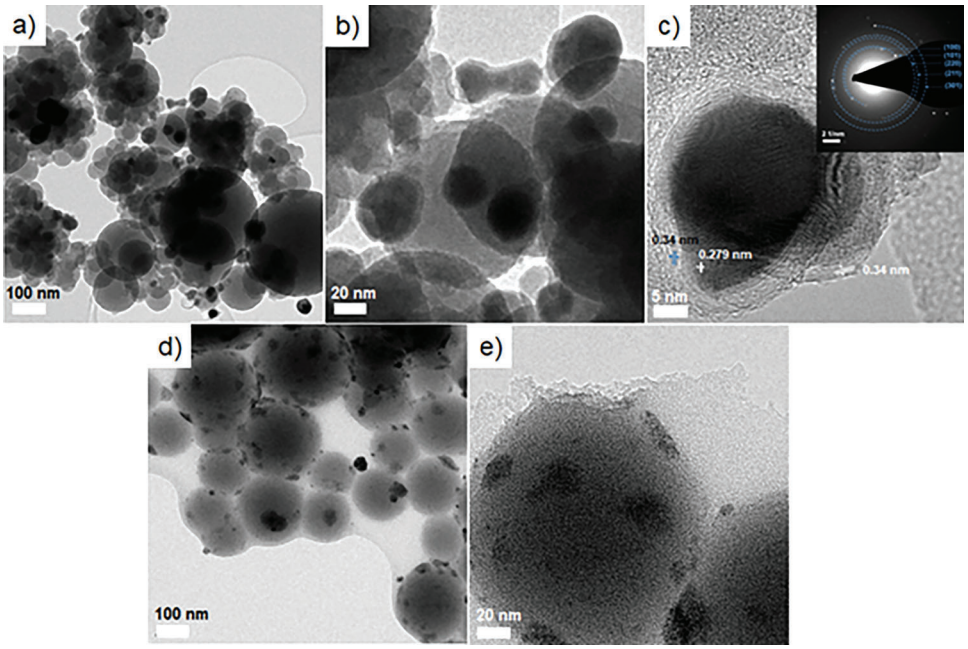

Figure 2. TEM images of a,b) SiOC-M2, and d,e) SiOC-H2. c) High-resolution TEM image of the SiOC-M2 sample shows the encapsulation of one Sn nanoparticle by several layers of turbostratic carbon. The corresponding SAED pattern for this Sn nanoparticle is shown in the insets.

based on IUPAC classification, while the SiOC-H1 and SiOC-H2 samples derived from PMPS polymer show Type II. In addition to the hysteresis loops, i.e., mesoporosity, all samples also show an increased N_2 adsorption at a high relative pressure ($p/p_0 > 0.8$), which might be due to the formation of macroporosity between particles. The calculated Brunauer–Emmett–Teller (BET) specific surface area (SSA) values of SiOC-M1 (39 $m^2\ g^{-1}$) and SiOC-M2 (36 $m^2\ g^{-1}$) were higher than that of the SiOC-H1 (10 $m^2\ g^{-1}$) and SiOC-H2 (8 $m^2\ g^{-1}$). These results agree with previous studies reported that the formation and stability of micro/mesoporosity in PDCs depend on the initial preceramic precursors and the amount and type of gaseous species (H_2, CO_2, CH_4, and other hydrocarbons, see later) released during the polymer-to-ceramic transformation process.[23–25]

While both M and H samples had similar external surface area values, it can be seen (see Figure S2, Supporting Information) from the particle size distribution data that M-samples comprise smaller particles in higher volume, contributing to the surface area rise. Besides, in previous work,[26] SiOC nanosized beads were formed via sol-gel chemistry using different initial precursors. The authors showed that while methyl-triethoxysilane-made samples maintained their spherical shape, phenyl-based precursors yielded a siloxane network with a lower glass transition temperature, preventing shape retention during pyrolysis. Similarly, phenyl-siloxane-based H-samples had a shape distortion, delivering ellipsoid-like forms and partial sintering in segregated areas. Accordingly, it is highly possible to assume that these samples experienced a partial pore closure, yielding different surface area values between M and H samples.

Polymer-to-ceramic transformation of Sn-containing PMS and PMPS polymeric precursor-made nanobeads were analyzed by thermogravimetry analysis (TGA) coupled with in situ mass spectrometry (MS) up to 1200 °C in Ar, and the data are given in **Figure 3**a,b. The most significant weight loss occurred between 400 and 800 °C because of the ceramization process.[25,27] Polymeric M1/M2 and H1/H2 beads had a weight loss of 18.1/19.4 and 35.6/42.3, corresponding to a final ceramic yield of 81.9%/80.6% and 64.4%/57.7% at the highest applied temperature (1200 °C).

According to in situ MS studies applied on the cured polymeric nanobeads, in the first step (from 200 to 360 °C), the release of H_2O (m/z = 18) and CO_2 (m/z = 44) occurred. Following that, during the second step between 360 and 680 °C, ceramization was indicated with the release of CH_3 (m/z = 15), CH_4 (m/z = 16), and C_2H_4 (m/z = 28). During the last step from 650 to 1100 °C, the transfer from polymer to ceramic was completed upon the release of H_2 (m/z = 2), CH_3 (m/z = 15), and CH_4 (m/z = 16).[27,28]

The Fourier transform infrared spectroscopy (FTIR) spectra of the SiOC samples are given in Figure S3b (Supporting Information). All SiOC samples obtained after pyrolysis at 1100 °C had a similar spectrum with Si—C and Si—O stretching vibration centering around 805 cm^{-1} and a broad peak belonging to the Si—O stretching due to Si—O—Si vibrations ≈1070 cm^{-1} of the SiOC network.[29,30]

The X-ray diffraction (XRD) patterns of SiOC ceramic nanobeads are shown in Figure 3c. While SiOC was expected to exhibit only broad diffuse scattering reflection for 2θ between 10° and 30°, related to amorphous silicate,[29,31] reflections attributed to metallic tin (ICDD PDF No. 01-086-2264) were observed in all SiOC samples analyzed. These results suggest that the used tin catalyst yielded metallic tin on the surface of SiOC nanobeads during pyrolysis.[12,16,17,32]

Raman spectroscopy (Figure 3d) was used to acquire information on the carbon phase dispersed within the SiOC matrix. When comparing SiOCs, it is possible to see two in-plane modes

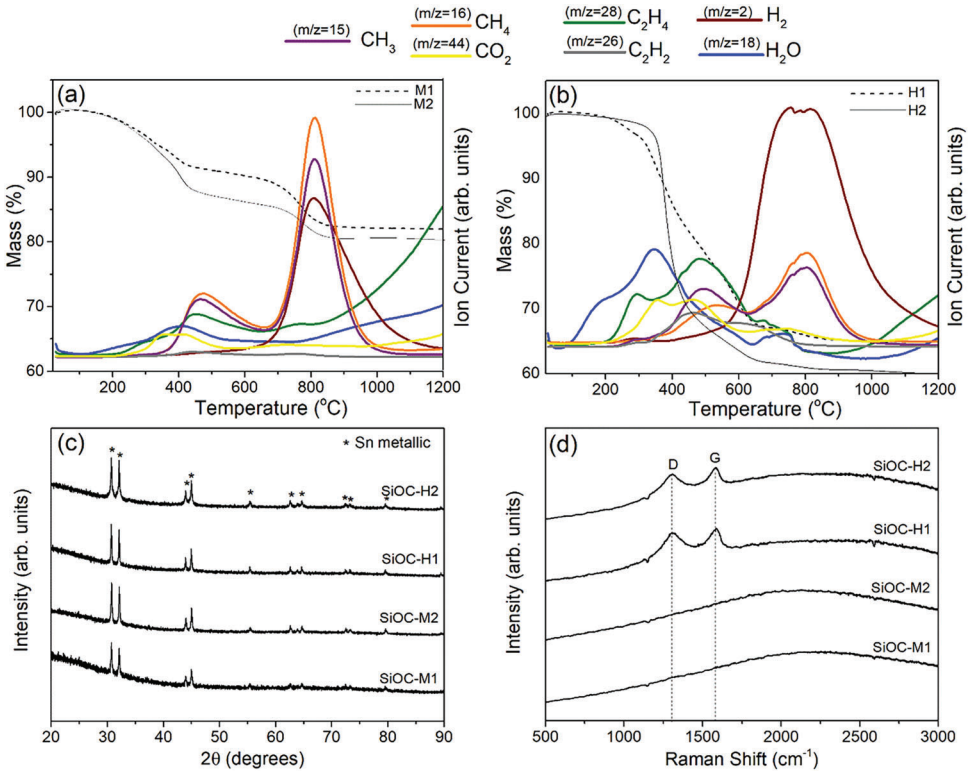

Figure 3. Results of simultaneous thermal gravimetric and mass spectrometry analysis of a) PMS-derived polymeric nanobeads and b) PMPS-derived polymeric nanobeads; c) XRD patterns of PMS and PMPS-derived SiOC/Sn ceramic nanobeads. At the top of the experimental data, reference reflection marks for metallic Sn (ICDD PDF No. 01-086-2264) are given; and d) Raman spectra of the PMS and PMPS-derived SiOC/Sn ceramic nanobeads.

only for high carbon SiOC samples (H1/H2): D-band and G-band around 1306 and 1584 cm^{-1}, respectively.[33,34] While pronounced fluorescence prevents the identification of the free carbon phase in SiOC obtained at lower pyrolysis temperatures (<1400 °C), it seems that the free carbon network was not developed well in the M samples compared to that of the H samples due probably to the reduction of the carbon precipitation caused by water during synthesis, and relatively low carbon in the used preceramic polymer, akin to previous data.[35,36]

Table 1 shows the elemental analysis results for all obtained SiOC/Sn ceramic nanobeads. The chemical formula normalized to 1 mole Si was quantified using literature.[37] All SiOC samples contained Sn, corroborating the XRD results (Figure 3c). The SiOC-M2 and SiOC-H2 samples prepared with a high concentration of tin catalyst (800 µL g^{-1} of resin) had higher Sn (5.9–6.3 wt%) in comparison with the SiOC-M1 and SiOC-H1 samples (i.e., 2.8–2.6 wt%) prepared with a lower catalyst concentration (400 µL g^{-1} of resin). These results suggest that the Sn content in the ceramics is linked to the concentration of the used tin catalyst.

In contrast, the amount of carbon content decreased in the SiOC-M2 and SiOC-H2 samples, compared with the SiOC-M1 and SiOC-H1, respectively, i.e., with increased Sn content. The tin oxide was expected to be formed first due to the thermal decomposition of Sn-containing preceramic precursor when temperature increased. The formed oxide was then reduced into the metallic Sn, causing the oxidation of carbon and silicon, aiding the formation of higher [SiO_4] units and reducing the carbon content.[16,17] As expected, the SiOC-H samples derived from C-rich PMPS polymer contained higher total carbon and free carbon than those in the SiOC-M samples. In other terms, higher Si and O were found in the SiOC-M samples.

Table 1. Chemical composition (neglecting the hydrogen) of the synthesized SiOC/Sn nanobeads. The explanation of the calculations of $SiC_zO_{2(1-z)}$, C_{free}, SiO_2, and SiC contents is given in the Experimental Section.

Sample	Elemental composition [wt%]				Chemical formula		Weight fraction [wt%]			
	Si	O	C	Sn	$SiC_zO_{2(1-z)}$	C_{free}	SiO_2	SiC	C_{free}	Sn
SiOC-M1	44.72	39.13	13.33	2.82	$SiO_{1.53}C_{0.23}$	0.46	73.47	14.83	8.88	2.82
SiOC-M2	49.06	33.86	11.16	5.92	$SiO_{1.21}C_{0.39}$	0.14	63.58	27.62	2.89	5.92
SiOC-H1	33.13	29.59	34.64	2.64	$SiO_{1.57}C_{0.22}$	2.23	55.58	10.23	31.56	2.64
SiOC-H2	38.18	30.02	25.53	6.27	$SiO_{1.37}C_{0.31}$	1.25	56.37	16.90	20.46	6.27

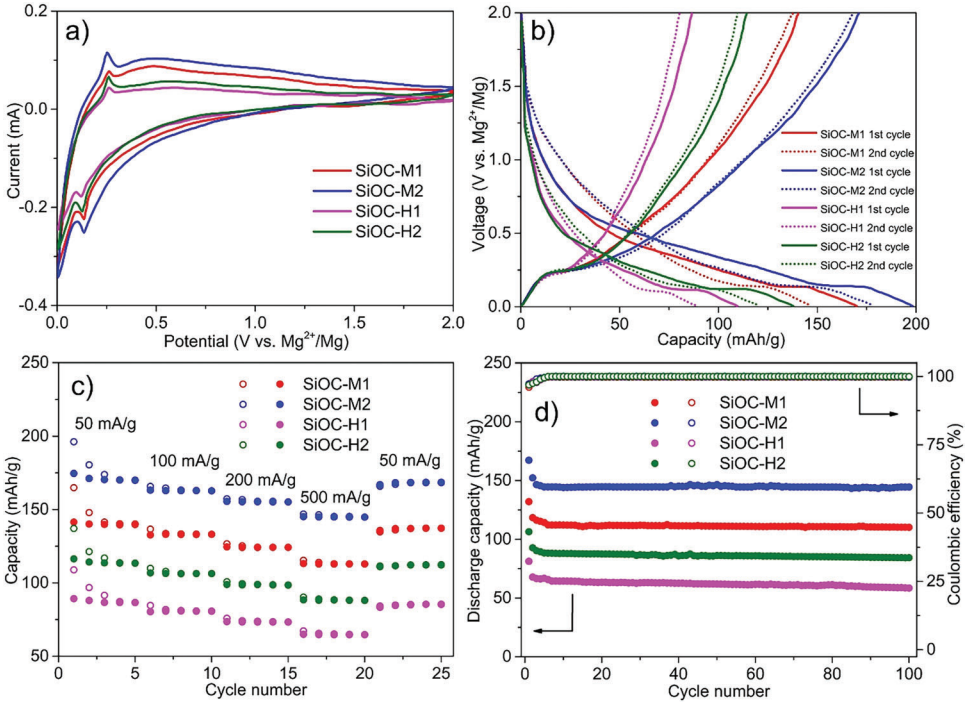

Figure 4. a) Cyclic voltammetry plots of SiOC-M1, SiOC-M2, SiOC-H1, and SiOC-H2 (second cycle); b) the charge–discharge profiles in the 0–2 V window (vs Mg/Mg^+) for the first and second cycle of SiOC-M1, SiOC-M2, SiOC-H1, and SiOC-H2 as magnesium battery anodes in $THF/PhMgCl/AlCl_3$ electrolyte at a current density of 50 mA g^{-1}; c) rate performances of SiOC-M1, SiOC-M2, SiOC-H1, and SiOC-H2 as magnesium battery anodes at different current rates in $THF/PhMgCl/AlCl_3$ electrolyte; d) cycling stability tests of SiOC-M1, SiOC-M2, SiOC-H1, and SiOC-H2 as magnesium battery anodes at different current rates in $THF/PhMgCl/AlCl_3$ electrolyte at a current density of 500 mA g^{-1}.

Figure 4 illustrates the results of the electrochemical tests, which are also summarized in Table S2 (Supporting Information). Before testing battery performances, CV tests were performed to evaluate the electrochemical activities. Figure 4a shows the recorded CV curves for the second cycle. Two electrochemical peaks can be observed at around 0.15 V (reduction peak) and 0.25 V (oxidation peak) on the cathodic and anodic sites, respectively, attributed to the magnesiation and de-magnesiation of Sn. As shown, the SiOC-M2 electrode exhibits the most significant specific current response, while the trend can be given as SiOC-M2 > SiOC-M1 > SiOC-H2 > SiOC-H1, similarly expected for the specific capacity.

Figure 4b depicts the galvanostatic discharge–charge profiles (first and second) at a current density of 50 mA g^{-1} in the 0–2 V window (vs Mg/Mg^{2+}). A considerable capacity loss in the first cycle was observed for all electrodes. This capacity loss has been commonly observed for most SiOC anodes in Li- and Na-ion batteries, explained by the irreversible insertion of these ions in SiOC. Besides, the formation of the solid-electrolyte interphase (SEI) layer on the electrode surface is due to the electrochemical reactions and decomposition of the electrolyte.[12,16,17,38] In accordance with CV curves, there were three noticeable voltage regions for the insertion of Mg^{2+} ions in the Sn/SiOC electrodes; two sloping voltage regions at low (<0.15 V) and high voltage (>0.25 V), separated by a plateau voltage region between 0.15 and 0.25 V. The two sloping voltage regions can be attributed to the insertion of Mg^+ ions into the micropores, defect sites, active chemical constituents, and between carbon layers. At the same time, the plateau region between 0.15 and 0.25 V could be assigned to the formation of Mg_2Sn.[39–43]

As seen in Figure 4b, the SiOC-M2 anode showed the highest first cycle magnesiation capacity (C_{mag}) of 198.2 mAh g^{-1}, compared to the SiOC-M1, SiOC-H1, and SiOC-H2 anodes that possess 164.9, 108.9, and 137.1 mAh g^{-1} capacities, respectively. The magnesiation capacity decreases in the order of SiOC-M2 > SiOC-M1 > SiOC-H2 > SiOC-H1, which agrees with the reducing order of the current response as revealed from the CV curves (Figure 4a). While the capacity difference between the Sn/SiOC samples could be attributed to the combination of factors, including microporosity, SSA, metallic Sn, and free carbon contents, it is still possible to speculate that the effect of Sn content was limited (M1 vs M2, and H1 vs H2). Instead, when the Sn content was invariable (M1 vs H1), and (M2 vs H2), the higher the microporosity (also SSA), and Si—O—C tetrahedral units, the higher the specific capacity was observed. This agrees with the difference observed in the sloping voltage regions if one compares the plateau voltage region attributed to the insertion of Mg^{2+} in metallic Sn (Figure 4b). The high SSA and porosity allow fast ion diffusion and accommodate the structural changes during the charging/discharging process.[4]

Mg^{2+} ion is smaller than Li^+ and Na^+, but its storage mechanisms in the SiOC matrix might be similar to those of Li^+ and Na^+ ions. These ions first occupy the available micropores in the SiOC matrix, followed by their insertion into the SiOC network.[44,45–48] This insertion might result in the cleavage of some Si—C or Si—O bonds, resulting in the expansion of the network for additional

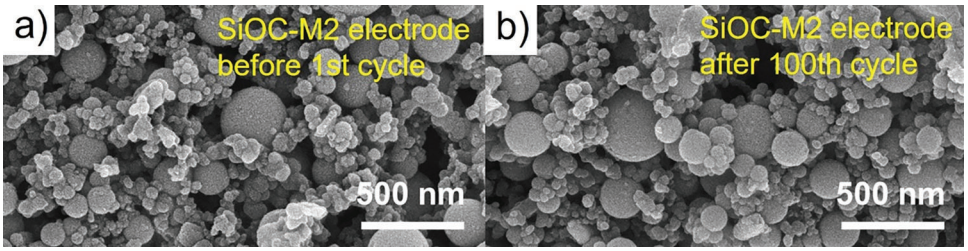

Figure 5. SEM images of SiOC-M2 electrode a) before the first cycle and b) after the 100th cycle. Note that the small-sized particulates seen between the beads are black carbon particles added as conductive agents in the electrode preparation process.

favorable sites for the subsequent ion insertion in SiOC.[44] However, the experimental storage capacity of SiOC for Mg^{2+} ions determined in this work is still much lower than those reported for Li^+ ions. Such an issue might be explained by the additional storage sites in SiOC for Li^+ ions due to the favorable formation of Li-rich Si compounds and Li-Si alloy compared to Na^+ and Mg^{2+} ions.[38,49,50] Incorporating Sn nanoparticles in the SiOC network not only increases the capacity by alloying with magnesium but also enhances the magnesium ion insertion in the SiOC network by facilitating the diffusion rate of Mg^{2+} ions, as also explained below.

Figure 4c compares rate test performances at charge/discharge different current densities. SiOC-M2 anode exhibited a superior rate capability among all electrodes with a discharge capacity of 170.0 mAh g^{-1} in the fifth cycle at the current density of 50 mA g^{-1}, decreasing to 162.8, 155.2, and 144.8 mAh g^{-1} with increasing the current density to 100, 200, and 500 mA g^{-1}, respectively. SiOC-H1 anode showed the lowest discharge capacity with 86.6 mAh g^{-1} in the fifth cycle at the current density of 50 mA g^{-1}, dropping to 80.8, 73.4, and 64.7 mAh g^{-1} with increasing the current density to 100, 200, and 500 mA g^{-1}, respectively. Moreover, when a low current density 50 mA g^{-1} was reapplied at the end of the high current series, the discharge capacity of 137.3, 168.4, 85.4, and 112.2 mAh g^{-1} was recovered for SiOC-M1, SiOC-M2, SiOC-H1, and SiOC-H2, respectively.

Figure 4d depicts the cycling performances and Coulombic efficiencies at the current density of 500 mA g^{-1}. The Coulombic efficiencies were almost 100% for all samples after several cycles. SiOC-M2 showed the highest stability of 144.5 mAh g^{-1} after 100 cycles with a capacity retention of 98.1%. As shown in Table S2 (Supporting Information), the Coulombic efficiency of Sn/SiOC anodes decreased in the order SiOC-M2 > SiOC-M1 > SiOC-H2 > SiOC-H1.

Figure 5a,b presents the SEM images of the best-performed sample, SiOC-M2, electrode before and after 100 cycles. The corresponding EDX mappings and XRD data after 100 cycles are shown in Figures S4 and S5 (Supporting Information). No surface or structural deterioration was observed on the electrode nanobeads after 100 cycles of charging/discharging, supporting the cycling stability test results (see Figure 4d) and suggesting that SiOC ceramic matrix prevented the collapse seen for other systems.[4,12,13,17]

Figure S6 (Supporting Information) gives the characterization and battery performance data of the SiOC-M2-ir sample. The sample comprises irregularly shaped micron-sized particles (Figure S6a, Supporting Information), but similar to others, it had metallic Sn as revealed by XRD analysis (Figure S6b, Supporting Information). In contrast to the SiOC-M2, the SiOC-M2-ir possessed a low SSA value of 0.31 m^2 g^{-1} (Figure S6c, Supporting Information); concurrently, it showed much lower battery performance compared to SiOC-M2, see Figure S6d,e (Supporting Information). Irregularly shaped SiOC particulates yielded a low capacity of 18 mAh g^{-1} and poor rate capability, indicating the importance of the microstructural characteristics.

To further investigate the mechanisms and kinetics of battery reactions, electrochemical impedance spectroscopy (EIS) measurements were conducted. **Figure 6**a presents EIS results at the current density of 50 mA g^{-1}, similarly summarized in **Table 2**. In Figure 6a, the depressed semicircles in the high-frequency region shown in all Nyquist plots represent the electrode–electrolyte interface charge-transfer resistance (R_{ct}). τ is the relaxation time constant of charge transfer, calculated from the frequencies at the minimum of the charge transfer semicircles in the high-frequency region with the equation $\tau = 1/2\pi f_{max}$ (f_{max} is the peak frequency of the semicircle in the high-frequency region).

As shown in Table 2, R_{ct} and τ values of SiOC-M samples were lower than the SiOC-H, implying that the SiOC-M samples present faster interface charge transfer than those of the SiOC-H group. These results could be explained by the higher SSA of the SiOC-M samples, allowing for lower interface polarization and faster interface reactions.[51] It was also noticed that the samples with higher tin content showed smaller R_{ct}/τ values, which could facilitate interface charge transfer due to its high metallic electrical conductivity.[12] Since R_{ct} and τ values are closely related to rate capability,[13] SiOC rate performances could be improved by increasing the microporosity, SSA, and tin content.

In the low-frequency region of Figure 6a, the slope represents the Warburg impedance (Z_w) caused by the diffusion of Mg^{2+} ions in the electrode, which can be calculated from Equation (1)[52]

$$Z_w = \sigma\omega^{-1/2} - j\sigma\omega^{-1/2} \quad (1)$$

where ω is the angular frequency ($\omega = 2\pi f$), and σ is the Warburg coefficient (calculated from the slope of the line $Z' \sim \omega^{-1/2}$). The cell diffusion process can be represented by the diffusion coefficient D, estimated based on the following Equation (2)[53]

$$D = \frac{R^2T^2}{2A^2n^4F^4C^2\sigma^2} \quad (2)$$

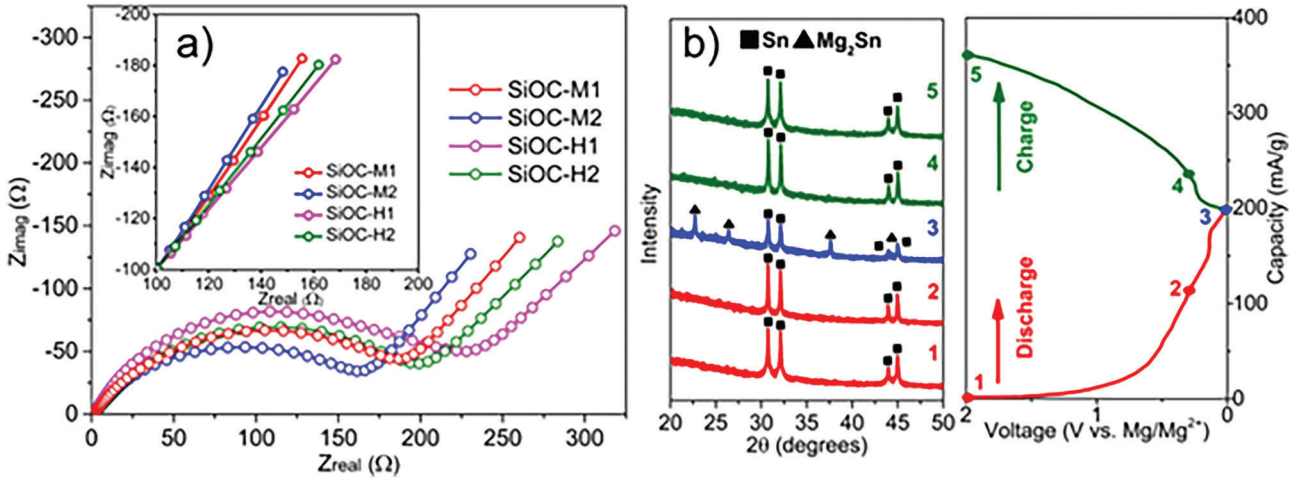

Figure 6. a) Nyquist impedance plots of SiOC-M1, SiOC-M2, SiOC-H1, and SiOC-H2 after pausing discharge at 0.5 V for 3 h; b) ex situ XRD patterns of SiOC-M2 anodes during the first magnesiation–demagnesiation cycle.

where A is the SSA of the electrode 2.011×10^{-4} m^2, n is the number of electrons per molecule attending the electronic transfer reaction, F is the Faraday constant 96 500 C mol^{-1}, C is the concentration of magnesium ion in the electrode ($C = \rho/M$), R is the gas constant 8314 J Kmol^{-1}, T is 293 K, and σ is the Warburg coefficient. From the results in Table 2, the Z_w of the electrodes increases in the order of SiOC-M2 < SiOC-M1 < SiOC-H2 < SiOC-H1, while the diffusion coefficient D gives reverse order. Higher SSA and porosity of the SiOC-M sample group aided the Mg^{2+} ion diffusion due probably to shortening diffusion pathways.[51]

From Figure 6a, the Warburg slope line of all electrodes has angles slightly higher than 45°, indicating that Faradaic Mg^{2+} intercalation in Sn/SiOC played a significant role in Mg^{2+} ion storage and the surface capacitive effects were present in all cells.[13] The higher slope angle means faster penetration of Mg^{2+} ions into electrodes due to more surface capacitive effects.[54] As discussed above, Mg^{2+} ions could be capacitively inserted in micropores of SiOC. In the inset of Figure 6a, the slope angle decreases in the order of SiOC-M2 > SiOC-M1 > SiOC-H2 > SiOC-H1, implying higher SSA and porosity of the SiOC matrix can contribute to faster Mg^{2+} ion diffusion because of more capacitive storage. Compared with the R_{ct} values, the Z_w values are close, indicating that the diffusion process is equally crucial in determining battery performances with the interface charge transfer process. In summary, the high SSA, porosity, and Sn content of the SiOC ceramic may decrease the Z_w and improve the battery performance.

Table 2. Characteristic parameters from impedance spectra from EIS measurement and the relaxation voltage preceding EIS measurement.

Samples	R_{ct} [Ω]	τ_{ct} [ms]	Z_w [Ω] (50 mHz)	D (Mg^{2+}) [cm^2 s^{-1}]
SiOC-M1	176	1.0 (159 Hz)	156	1.32×10^{-11}
SiOC-M2	151	0.8 (198 Hz)	133	1.81×10^{-11}
SiOC-H1	209	1.5 (106 Hz)	193	8.64×10^{-12}
SiOC-H2	183	1.1 (145 Hz)	176	1.04×10^{-11}

The results of EIS measurements for the SiOC-M1, SiOC-M2, SiOC-H1, and SiOC-H2 electrodes after 100 cycles at 500 mA g^{-1} are shown in Figure S7 and Table S3 (Supporting Information) for comparison. Similar to the results before cycling, SiOC-M2 shows the smallest impedance value, and SiOC-H1 presents the highest impedance value. The SiOC-M2 exhibits a small increase of both charge-transfer resistance (R_{ct}) and diffusion impedance (Z_w) before and after cycling, confirming the good structural stability as revealed by cycling stability test (Figure 4d), SEM and XRD characterizations (Figure 5 and Figures S4 and S5, Supporting Information).

To validate the alloying between magnesium and tin in the Sn/SiOC electrode, ex situ XRD measurements were conducted on the SiOC-M2 anode at various charge states at a current density of 50 mA g^{-1}. As shown in Figure 6b, the XRD reflections corresponding to the Mg_2Sn phase (ICDD PDF No. 07-0274) appeared when the discharging curve reached the end in the first cycle (after the small plateau at 0.15 V). When the battery is recharged after the small obscure plateau at around 0.25 V, the Mg_2Sn XRD peaks disappear. Besides, no other XRD peaks can be observed. The magnesiation plateau observed at around 0.15 V corresponds to the formation of Mg_2Sn based on the electrochemical reaction shown in Equation (3)[40]

$$Sn + 2Mg^{2+} + 4e^- \rightarrow Mg_2Sn \quad (3)$$

The plateau observed at around 0.25 V corresponds to the extraction of Mg^{2+} from Mg_2Sn, indicating that the storage mechanism Mg^{2+} into the Sn/SiOC was capacitive through the micropores and via intercalation with metallic Sn. The observations aligned with previously reported works investigating Sn-based electrodes for magnesium-ion batteries.[39,40–43] In addition, the voltage required to extract Mg^{2+} from Mg_2Sn was only 0.1 V more positive than the voltage needed to insert Mg^{2+} into Sn. Such low hysteresis suggests the introduction of Sn in the SiOC ceramic matrix may decrease the electrode polarization and improve the battery performance analogous to the electrochemical performance results discussed above.[55]

Table 3. Summary of the electrochemical performance of recently reported anode materials for magnesium-ion batteries and the comparison with this work.

Material	Reversible capacity [mAh g^{-1}]	Cycles	Power density [W kg^{-1}]	Energy density [Wh kg^{-1}]	Reference
Sn	25	50	10	24	[36]
Eutectic Bi-Sn	133	200	81	105	[39]
Mg_2Sn	115	50	31	49	[52]
Bi	170	150	45	–	[50]
Mg_3Bi_2	109	200	69	102	[51]
In	125	10	17	23	[49]
MgIn	140	6	22	34	[49]
SnSb/graphite	300	200	105	84	[53]
SiOC-M2 (this work)	144.5 (500 mA g^{-1})	100	232	124	–

SiOC-M2 anode was additionally analyzed by X-ray photoelectron spectroscopy (XPS), see Figure S8 (Supporting Information). Mg 1s, 2s, and 2p peaks appeared at 1303.8, 89.3, and 50.4 eV, respectively, in the XPS spectra after magnesiation. Such peaks, corresponding to Mg_2Sn alloy, disappeared after the battery demagnesiation. Moreover, as shown in Figure S9 (Supporting Information), the Sn $3d_{5/2}$ spectra, before magnesiation, can be deconvoluted into two peaks at 484.63 and 486.92 eV, corresponding to Sn^0 and SnO_2, respectively. The latter, which was due to the high oxidation tendency of Sn, i.e., surface oxidation, has already been discussed in the literature,[56,57] as others reported the detection of metal oxides on the surface of metal-containing SiOC composites via XPS.[58] The peak corresponding to Sn^0 is shifted to lower binding energy (484.2 eV) after magnesiation due to the formation of Mg_2Sn,[59] before shifting to higher binding energy again after demagnesiation (i.e., formation of metallic Sn^0 again). The results corroborate the ex situ XRD data from magnesiation-demagnesiation cycle (see Figure 6b).

As shown in **Table 3**, SiOC/Sn nanobeads synthesized in this work exhibit excellent battery performance for magnesium-ion batteries compared with the recently reported anode materials.[39,41,60–64] SiOC reveals at least two advantages. The first is the excellent reversible capacity after many cycles, i.e., the demand for practical battery use. The second is the much higher power and energy density, essential for many practical applications like electric vehicles and grid energy storage. Future work could focus on determining the appropriate Sn/SiOC ratio with tunable microstructure and morphology.

3. Conclusions

Polymer-derived ceramic SiOC/Sn nanobeads with different carbon/tin contents were synthesized and tested as an anode in magnesium-ion batteries for the first time. Results of battery performance tests presented the highest capacity of 198.2 mAh g^{-1} after the first discharging and a reversible capacity of 144.5 mAh g^{-1} after 100 cycles. Excellent rate capability efficiency of 85.2% was achieved. Various factors influenced battery performances, including microporosity, SSA, metallic Sn, and free carbon contents. EIS, CV tests, and ex situ XRD measurements revealed that enhanced surface area contributed to higher capacity by providing more accessible Mg^{2+} ion storage sites and higher rate capability via improving the diffusion process. While the resistivity of the samples ranged from ≈150 to 210 Ω, and the Warburg impedance values from 133 to 193 Ω (50 mHz), the highest diffusion constant (D_{Mg2+}) was observed as 1.81×10^{-11} cm^2 s^{-1} from the sample having the highest surface area and tin content. The formation of magnesium stannide (Mg_2Sn), and reversible electrochemical Mg^+ extraction/insertion occurring in the polymer-derived SiOC nanobead matrices were additionally demonstrated.

4. Experimental Section

Materials: For ceramics synthesis: two economic, commercially available silicon resins with different compositions in terms of total carbon content—PMS and PMPS, respectively (Wacker GmbH, Burghausen, Germany) were used as low and high carbon SiOC precursors. Deionized water (Ultrapure Type-I, 18.2 MΩ cm at 25°C, Millipak Direct-Q 8 UV water purification system) and surfactant (Pluronic F127, Sigma, CAS: 9003-11-6, USA) were used. Toluene (Merck, EMSURE grade, CAS: 108-88-3, Germany) and xylene (ACS reagent ≥ 99.8%, Merck, CAS:1330-20-7, Germany) were used as solvents. Tin(II) 2-ethylhexanoate (Sigma-Aldrich, CAS: 301-10-0, USA) was used as a catalyst and source for the in situ formation of tin in the SiOC matrix after pyrolysis.

For battery testing: nickel (99.9%) and magnesium (99.9%) foils were acquired from Goodfellow. Phenylmagnesium chloride solution (PhMgCl; 2.0 M in THF), anhydrous $AlCl_3$, and Whatman glass fiber filter paper (GF/A) were ordered from Sigma Aldrich. Carbon black, anhydrous tetrahydrofuran (THF), and 1-methyl-2-pyrrolidinone (NMP) were purchased from Alfa Aesar. Coin cell cases (CR2032) were obtained from Mitsubishi.

Synthesis of Sn-Containing SiOC Nanobeads: Tin-containing silicon oxycarbide ceramic nanobeads (Sn/SiOC) were synthesized via the oil in water (o/w) emulsion method by using silicon resins (PMS and PMPS). Detailed synthesis procedure can be found elsewhere;[30] briefly, 80 mL of deionized (DI) water and 0.8 g of surfactant were mixed in a typical synthesis. 5 g of silicon resin and 7 mL of toluene were mixed in another beaker. Then the oil phase was added to the water phase. An ultrasonic probe sonication (QSonica, Q500 system Sonicator, Newtown, CT) with 50% amplitude (for 5 min, 5 s on/off) was applied to obtain an emulsion. Different amounts (400 and 800 µL) of diluted catalysts (15 vol% in xylene) were used per gram of silicon resin. The curing was conducted for 18 h at 150 °C in an atmospheric oven, followed by pyrolysis at 1100 °C in an alumina tube furnace under Ar flow with a heating rate of 2 °C min^{-1}, a flow rate of 200 mL min^{-1}, and 2 h dwelling time. While the effect of processing parameters on the size alteration was not the focus in the present

work, it is possible to tailor it via time/amplitude change and/or catalyst amount. Depending on the silicon resin used for SiOC nanobeads synthesis, samples are labeled "M" and "H" for those prepared by using PMS (low carbon content) and PMPS (high carbon content) as preceramic polymers, respectively. The related sample codes were listed in Table S1 (Supporting Information); accordingly, preceramic polymer types and tin catalyst per gram of silicon resin for synthesized SiOC nanobeads in this research (400/resin (μL g^{-1}) was named SiOC-M1 and SiOC-H1; 800/resin (μL g^{-1}) was named SiOC-M2 and SiOC-H2). The sample SiOC-M2-ir, is the same material SiOC-M2 but not having spherical morphology; instead, it comprises irregularly shaped particulates prepared merely for comparison. SiOC-M2-ir was produced by mixing (via magnetic stirrer) identical amounts of silicon resin, toluene, and tin catalyst, followed by the same curing and pyrolysis schedule used for emulsion-made spherical particles.

Characterization: TGA-MS) was performed for the polymeric beads on an STA 409 PC LUXX (Netzsch, Selb, Germany) connected with a mass spectrometer OMNi Star GSD 320 (Pfeiffer Vacuum, Asslar, Germany) with a heating rate of 5 °C min^{-1} in inert Ar atmosphere.

Attenuated total reflectance Fourier transform infrared spectroscopy (ATR-FTIR) measurements of the synthesized Sn-containing SiOC ceramic nanocomposites were measured from 4000 to 450 cm^{-1} in glove box using Nicolet iS5 (Thermo Fisher Scientific, MA, USA) and Specac Golden Gate (Waltham, MA) with a diamond plate.

XRD patterns were collected using a Bruker D8 diffractometer (AXS D8 ADVANCE X-ray diffractometer, Bruker, Billerica, MA) equipped with Cu$K\alpha$ radiation ($\lambda = 0.154$ nm) over 2θ range from 20° to 90° using step counting time of 3 s and scanning rate of 0.05°.

XPS measurements were conducted on an ESCALAB 250Xi instrument (Thermo Fisher Scientific, Waltham, MA). The X-ray spot size was 100 m. Powders were sprinkled on the carbon conductive tape in the glove box to prepare samples for analysis. The C 1s core line with a binding energy of 284.8 eV was used to calibrate all XPS spectra. The data were processed by using XPS Peak software. The Lorentzian–Gaussian ratios in peak fitting have been constrained between 20 and 30. Shirley backgrounds were used in all fittings.

Raman spectroscopic measurements were performed in backscattering configuration with optical excitation at a wavelength of 473 nm (solid-state laser). A microscope objective focused the incident laser light onto the surface of the sample powder (spot diameter of ≈1 μm). The backscattered light was collected by the same purpose (confocal configuration), spectrally dispersed by an 80-cm spectrograph (LabRam HR Evolution, Horiba/Jobin Yvon, Palaiseau, France), and detected with a liquid-nitrogen-cooled charge-coupled device (CCD). A bandpass filter with ultra-narrow spectral bandwidth was used for Rayleigh light suppression.

Morphological characterization of samples was performed using a SEM (FEI Quanta 250 FEG, Hillsboro, OR) coupled with an EDX detector (Thermo Fisher Scientific, MA, USA). All samples were sputter-coated with ≈4 nm layer of Au (Emitech K550X sputter coater, Quorum Technologies, Laughton, East Sussex, UK) before the SEM characterization. Average sample particle size was then obtained from 100 measurements using the ImageJ software (ImageJ 1.52a, National Institutes of Health, USA) applied to the SEM images. The stereological equation Dsphere = Dcircle/0.78566 was then used to convert the data to 3D.[29]

TEM images of the Sn/SiOC nanospheres were acquired using FEI TECNAI G^2 20 S-TWIN equipped with a LaB6-source at 200 kV acceleration voltage (Hillsboro, OR). High-resolution transmission electron microscopy (HRTEM) images were acquired using a 300 kV cold FEG and probe-corrected JEM-ARM300F2 from JEOL Ltd. (Freising, Germany). Samples were prepared by dispersing the Sn/SiOC powders in ethanol using ultrasonication, followed by dropping them onto a copper grid covered with carbon film.

Nitrogen sorption was applied using a QuadraSorb Station 4 apparatus (Quantachrome, Boynton Beach, FL). Isotherms were recorded at 77 K after degassing under a vacuum at 200 °C for 24 h before the measurement. The SSA was acquired using BET calculations.

Elemental analyses for silicon (Si) and tin (Sn) were performed with inductively coupled plasma optical emission spectroscopy (ICP-OES) by using a Horiba Scientific ICP Ultima2 (Horiba, Kyoto, Japan). Prior to analyses, powder samples were digested in an aqueous suspension of HNO_3 and HF acid mixture at 200 °C for 5 h in a Teflon-lined autoclave. The carbon contents of the synthesized samples were measured by a Carbon analyzer CS744 (Leco Corporation, MI, USA). The weight fraction of oxygen was calculated as the difference to 100 wt% of the sum of the wt% values of C, Si, and Sn, assuming no other elements were present in the samples. The chemical composition of synthesized materials was normalized to 1 Si (i.e., SiO_xC_y). The free carbon content in the samples was determined considering the chemical formula $SiC_zO_{2(1-z)}$ for the matrix, where the mole fraction of free carbon (mC_{free}) = $C_y - C_z$. The mole fraction of SiC, SiO_2, and C_{free} in the samples was calculated considering the composition of the synthesized samples as nSiC:(1−n)SiO_2:mC_{free}, where n (i.e., 1−0.5x) refers to the ratio of SiC to SiO_2, and m (i.e., $0.5x + y - 1$) is the mole fraction of free carbon.[37]

Battery assembling procedures were conducted in an argon-filled glove box following previously reported guidelines.[65] Coin cell cases, spacers, springs, and o-rings produced by Mitsubishi were used. A slurry of 80 wt% active material, 10 wt% Super-P carbon black, and 10 wt% polyvinylidene fluoride dispersed in NMP were prepared by wet grinding for 1 h. For fabrication of the working electrodes, this slurry was then tape-cast on nickel foil and dried, first in the air at 50 °C and then under vacuum at 100 °C. The resulting mass loading of the active electrode material was 1.2 mg cm^{-2}. The coated working electrodes were then pressed at a pressure of 80–120 kg cm^{-2} and were cut into circular forms of 14 mm in diameter. Magnesium foil with a diameter of 16 mm and a thickness of 0.25 mm was adopted as the counter electrode. GF/A was adopted as a cell separator.

The electrolyte was synthesized in a glove box under Ar following the procedure described in refs.[19,65] First, 1.34 g $AlCl_3$ was added slowly to 15 mL THF solvent under vigorous stirring to obtain the targeted concentration. Subsequently, the acquired solution was dropwise added to a 10 mL PhMgCl/THF solution (2.0 M PhMgCl), followed by stirring for 16 h at room temperature (RT).

CV tests were carried out in assembled coin cells on a CHI660D electrochemical workstation (Chenhua, Shanghai, China) in the potential range of 0–2 V and at the scanning rate of 0.1 mV s^{-1}.

Battery performance tests were conducted using a CT2001A battery tester system (Wuhan LAND, Wuhan, China). Galvanostatic discharge–charge measurements were performed in the potential range of 0.05–2 V versus Mg^{2+}/Mg. Data points were collected every 3 s. The battery cycling stability tests were conducted at a current density of 500 mA g^{-1} for 100 cycles. The following current densities were applied for the rate performance tests: 5 × 50, 5 × 100, 5 × 200, and 5 × 500 mA g^{-1} followed by 5 × 50 mA g^{-1}.

EIS measurements were conducted on coin cells with SiOC-M2 anodes using a Gamry EIS box (Gamry, PA, USA) in potentiostatic mode with 5 mV amplitude between 50 mHz and 1 MHz. The cell was discharged to 5 mV and then charged to 2.0 V at a current density of 50 mA g^{-1}. Cells were discharged and charged with pausing intervals at specific cell potentials (0.5, 1.0, 1.5, and 2.0 V) and were relaxed for 3 h before EIS measurements. *Ex situ* XRD characterization was additionally performed on the electrode materials at different states of charge/discharge by stopping battery cycling and taking out anodes during the discharging (2, 0.3, and 0 V) and charging (0, 0.3, and 2 V) process.

Supporting Information

Supporting Information is available from the Wiley Online Library or from the author.

Acknowledgements

Funding for open access charge: TUBITAK-ULAKBIM, Turkiye. This research was funded by China Scholarship Council (201606280048). This research was funded by the Alexander von Humboldt (AvH) Foundation. W.G. acknowledges the financial support from the China Scholarship Council. C.V.A. acknowledges the support of the Alexander von Humboldt

(AvH) Foundation. Cekdar Vakif Ahmetoglu and Oyku Icin acknowledge the Izmir Institute of Technology, The Center for Materials Research.

Conflict of Interest

The authors declare no conflict of interest.

Author Contributions

W.G.: conceptualization, methodology, investigation, data curation, writing – original draft; O.I.: investigation, writing – review and editing; C.V.: conceptualization, writing – original draft, review and editing, supervision, funding acquisition; D.K.: methodology, investigation, data curation; A.G.: supervision, writing – review and editing, resources; M.F.B.: conceptualization, writing – review and editing, supervision, project administration. All authors have read and agreed to the published version of the manuscript.

Data Availability Statement

The data that support the findings of this study are available from the corresponding author upon reasonable request.

Keywords

anodes, energy storage, magnesium batteries, silicon oxycarbide

Received: May 4, 2023
Revised: July 24, 2023
Published online: September 10, 2023

[1] M. Weiss, R. Ruess, J. Kasnatscheew, Y. Levartovsky, N. R. Levy, P. Minnmann, L. Stolz, T. Waldmann, M. Wohlfahrt-Mehrens, D. Aurbach, M. Winter, Y. Ein-Eli, J. Janek, *Adv. Energy Mater.* **2021**, *11*, 2101126.
[2] M. Ge, C. Cao, G. M. Biesold, C. D. Sewell, S.-M. Hao, J. Huang, W. Zhang, Y. Lai, Z. Lin, *Adv. Mater.* **2021**, *33*, 2004577.
[3] X. Zhao, V. P. Lehto, *Nanotechnology* **2021**, *32*, 042002.
[4] Q. Wen, F. Qu, Z. Yu, M. Graczyk-Zajac, X. Xiong, R. Riedel, *J. Adv. Ceram.* **2022**, *11*, 984.
[5] G. Shao, D. A. H. Hanaor, J. Wang, D. Kober, S. Li, X. Wang, X. Shen, M. F. Bekheet, A. Gurlo, *ACS Appl. Mater. Interfaces* **2020**, *12*, 46045.
[6] G. Mera, A. Navrotsky, S. Sen, H. J. Kleebe, R. Riedel, *J. Mater. Chem. A* **2013**, *1*, 3826.
[7] M. Wilamowska-Zawlocka, P. Puczkarski, Z. Grabowska, J. Kaspar, M. Graczyk-Zajac, R. Riedel, G. D. Sorarù, *RSC Adv.* **2016**, *6*, 104597.
[8] V. S. Pradeep, D. G. Ayana, M. Graczyk-Zajac, G. D. Soraru, R. Riedel, *Electrochim. Acta* **2015**, *157*, 41.
[9] V. S. Pradeep, M. Graczyk-Zajac, R. Riedel, G. D. Soraru, *Electrochim. Acta* **2014**, *119*, 78.
[10] R. Riedel, G. Mera, R. Hauser, A. Klonczynski, *J. Ceram. Soc. Jpn.* **2006**, *114*, 425.
[11] B. Krüner, C. Odenwald, N. Jäckel, A. Tolosa, G. Kickelbick, V. Presser, *ACS Appl. Energy Mater.* **2018**, *1*, 2961.
[12] J. Wang, D. Kober, G. Shao, J. D. Epping, O. Görke, S. Li, A. Gurlo, M. F. Bekheet, *Mater. Today Energy* **2022**, *26*, 100989.
[13] C. Shi, H. Huang, Y. Xia, J. Yu, R. Fang, C. Liang, J. Zhang, Y. Gan, W. Zhang, *Chemistry* **2019**, *25*, 7719.
[14] K. Kravchyk, L. Protesescu, M. I. Bodnarchuk, F. Krumeich, M. Yarema, M. Walter, C. Guntlin, M. V. Kovalenko, *J. Am. Chem. Soc.* **2013**, *135*, 4199.
[15] J. Gonzalez, K. Sun, M. Huang, S. Dillon, I. Chasiotis, J. Lambros, *J. Power Sources* **2015**, *285*, 205.
[16] R. J. C. Dubey, P. V. W. Sasikumar, F. Krumeich, G. Blugan, J. Kuebler, K. V. Kravchyk, T. Graule, M. V. Kovalenko, *Adv. Sci.* **2019**, *6*, 1901220.
[17] J. Kaspar, C. Terzioglu, E. Ionescu, M. Graczyk-Zajac, S. Hapis, H.-J. Kleebe, R. Riedel, *Adv. Funct. Mater.* **2014**, *24*, 4097.
[18] D. H. Youn, A. Heller, C. B. Mullins, *Chem. Mater.* **2016**, *28*, 1343.
[19] J. Muldoon, C. B. Bucur, T. Gregory, *Chem. Rev.* **2014**, *114*, 11683.
[20] A. Ponrouch, J. Bitenc, R. Dominko, N. Lindahl, P. Johansson, M. R. Palacin, *Energy Storage Mater.* **2019**, *20*, 253.
[21] C. B. Bucur, T. Gregory, A. G. Oliver, J. Muldoon, *J. Phys. Chem. Lett.* **2015**, *6*, 3578.
[22] M. Scheffler, T. Gambaryan-Roisman, T. Takahashi, J. Kaschta, H. Muenstedt, P. Buhler, P. Greil, *Ceram. Trans.* **2000**, *115*, 239.
[23] J. Wang, A. Gili, M. Grünbacher, S. Praetz, J. D. Epping, O. Görke, G. Schuck, S. Penner, C. Schlesiger, R. Schomäcker, A. Gurlo, M. F. Bekheet, *Mater. Adv.* **2021**, *2*, 1715.
[24] J. Wang, M. Grünbacher, S. Penner, M. F. Bekheet, A. Gurlo, *Polymers* **2022**, *14*, 1.
[25] C. Vakifahmetoglu, P. Colombo, S. M. Carturan, E. Pippel, J. Woltersdorf, *J. Am. Ceram. Soc.* **2010**, *93*, 3709.
[26] S. Dirè, V. Tagliazucca, L. Salvadori, G. D. Sorarù, *J. Am. Ceram. Soc.* **2011**, *94*, 3819.
[27] J. Wang, V. Schölch, O. Görke, G. Schuck, X. Wang, G. Shao, S. Schorr, M. F. Bekheet, A. Gurlo, *Open Ceram.* **2020**, *1*, 100001.
[28] M. Hojamberdiev, R. M. Prasad, C. Fasel, R. Riedel, E. Ionescu, *J. Eur. Ceram. Soc.* **2013**, *33*, 2465.
[29] T. Semerci, M. D. D. Innocentini, G. A. Marsola, P. R. O. Lasso, G. D. Soraru, C. Vakifahmetoglu, *ACS Appl. Polym. Mater.* **2020**, *2*, 4118.
[30] O. Icin, C. Vakifahmetoglu, *Ceram. Int.* **2021**, *47*, 27050.
[31] L. Guo, Q. Ma, Z. Hu, C. Xu, *Ceram. Int.* **2021**, *47*, 21815.
[32] S. E. Wang, J.-S. Park, M. J. Kim, Y. C. Kang, D. S. Jung, *Appl. Surf. Sci.* **2022**, *589*, 152952.
[33] S. K. Ramasahayam, U. B. Nasini, V. Bairi, A. U. Shaikh, T. Viswanathan, *RSC Adv.* **2014**, *4*, 6306.
[34] C. Vakifahmetoglu, V. Presser, S.-H. Yeon, P. Colombo, Y. Gogotsi, *Microporous Mesoporous Mater.* **2011**, *144*, 105.
[35] A. Tolosa, B. Krüner, N. Jäckel, M. Aslan, C. Vakifahmetoglu, V. Presser, *J. Power Sources* **2016**, *313*, 178.
[36] C. Vakifahmetoglu, M. Balliana, P. Colombo, *J. Eur. Ceram. Soc.* **2011**, *31*, 1481.
[37] G. D. Sorarù, L. Pederiva, J. Latournerie, R. Raj, *J. Am. Ceram. Soc.* **2002**, *85*, 2181.
[38] C. Chandra, H. S. Cahyadi, S. Alvin, W. Devina, J.-H. Park, W. Chang, K. Y. Chung, S. K. Kwak, J. Kim, *Chem. Mater.* **2020**, *32*, 410.
[39] F. Nacimiento, M. Cabello, C. Pérez-Vicente, R. Alcántara, P. Lavela, G. F. Ortiz, J. L. Tirado, *Nanomaterials* **2018**, *8*, 501.
[40] N. Singh, T. S. Arthur, C. Ling, M. Matsui, F. Mizuno, *Chem. Commun.* **2013**, *49*, 149.
[41] M. Song, J. Niu, K. Yin, H. Gao, C. Zhang, W. Ma, F. Luo, Z. Peng, Z. Zhang, *Nano Res.* **2019**, *12*, 801.
[42] M. Song, Y. Wang, C. Si, W. Cui, W. Yang, G. Cheng, Z. Zhang, *Sci. China: Chem.* **2022**, *65*, 1433.
[43] A. B. Ikhe, S. C. Han, S. J. R. Prabakar, W. B. Park, K. S. Sohn, M. Pyo, *J. Mater. Chem. A* **2020**, *8*, 14277.
[44] C. Chandra, W. Devina, H. S. Cahyadi, S. K. Kwak, J. Kim, *Chem. Eng. J.* **2022**, *428*, 131072.
[45] M. Weinberger, P. H. Su, H. Peterlik, M. Lindén, M. Wohlfahrt-Mehrens, *Nanomaterials* **2019**, *9*, 1.

[46] J. Kaspar, M. Storch, C. Schitco, R. Riedel, M. Graczyk-Zajac, *J. Electrochem. Soc.* **2016**, *163*, A156.
[47] C. Chandra, J. Kim, *Chem. Eng. J.* **2018**, *338*, 126.
[48] X. Dou, D. Buchholz, M. Weinberger, T. Diemant, M. Kaus, S. Indris, R. J. Behm, M. Wohlfahrt-Mehrens, S. Passerini, *Small Methods* **2019**, *3*, 1800177.
[49] S. C. Jung, D. S. Jung, J. W. Choi, Y.-K. Han, *J. Phys. Chem. Lett.* **2014**, *5*, 1283.
[50] C. Tang, Y. Liu, C. Xu, J. Zhu, X. Wei, L. Zhou, L. He, W. Yang, L. Mai, *Adv. Funct. Mater.* **2018**, *28*, 1704561.
[51] L. A. Middlemiss, A. J. R. Rennie, R. Sayers, A. R. West, *Energy Rep.* **2020**, *6*, 232.
[52] W. Choi, H.-C. Shin, J. M. Kim, J.-Y. Choi, W.-S. Yoon, *J. Electrochem. Sci. Technol.* **2020**, *11*, 1.
[53] X. Wang, H. Hao, J. Liu, T. Huang, A. Yu, *Electrochim. Acta* **2011**, *56*, 4065.
[54] G. Wang, Y. Sun, D. Li, W. Wei, X. Feng, K. Müllen, *Small* **2016**, *12*, 3914.
[55] B. Lu, Y. Song, Q. Zhang, J. Pan, Y. T. Cheng, J. Zhang, *Phys. Chem. Chem. Phys.* **2016**, *18*, 4721.
[56] K. Xia, L. Qu, X. Liu, H. Han, Z. Hou, Y. Li, S. Deng, *Appl. Surf. Sci.* **2020**, *506*, 144775.
[57] S. Y. Turishchev, O. A. Chuvenkova, E. V. Parinova, D. A. Koyuda, R. G. Chumakov, M. Presselt, A. Schleusener, V. Sivakov, *Results Phys.* **2018**, *11*, 507.
[58] Y. Lee, K. Y. Lee, W. Choi, *Adv. Funct. Mater.* **2017**, *27*, 1702607.
[59] J. Tejeda, M. Cardona, N. J. Shevchik, D. W. Langer, E. Schönherr, *Phys. Status Solidi B* **1973**, *58*, 189.
[60] F. Murgia, E. T. Weldekidan, L. Stievano, L. Monconduit, R. Berthelot, *Electrochem. Commun.* **2015**, *60*, 56.
[61] K. V. Kravchyk, L. Piveteau, R. Caputo, M. He, N. P. Stadie, M. I. Bodnarchuk, R. T. Lechner, M. V. Kovalenko, *ACS Nano* **2018**, *12*, 8297.
[62] Y.-H. Tan, W.-T. Yao, T. Zhang, T. Ma, L.-L. Lu, F. Zhou, H.-B. Yao, S.-H. Yu, *ACS Nano* **2018**, *12*, 5856.
[63] D.-T. Nguyen, S.-W. Song, *J. Power Sources* **2017**, *368*, 11.
[64] Y. Cheng, Y. Shao, L. R. Parent, M. L. Sushko, G. Li, P. V. Sushko, N. D. Browning, C. Wang, J. Liu, *Adv. Mater.* **2015**, *27*, 6598.
[65] W. Guo, D. A. H. Hanaor, D. Kober, J. Wang, M. F. Bekheet, A. Gurlo, *Batteries* **2022**, *8*, 116.